

Interlayer exciton condensates between second Landau level orbitals in double bilayer graphene

Zeyu Hao,^{1,2,3,*} A. M. Zimmerman,³ Kenji Watanabe,⁴ Takashi Taniguchi,⁵ and Philip Kim^{3,†}

¹*Lawrence Berkeley National Laboratory, Berkeley, California 94720, USA*

²*Department of Electrical Engineering and Computer Sciences, University of California, Berkeley, California 94720, USA*

³*Department of Physics, Harvard University, Cambridge, Massachusetts 02138, USA*

⁴*Research Center for Functional Materials, National Institute for Material Science, 1-1 Namiki, Tsukuba 305-0044, Japan*

⁵*International Center for Materials Nanoarchitectonics, National Institute for Material Science, 1-1 Namiki, Tsukuba 305-0044, Japan*

Abstract

We present Coulomb-drag measurements on a heterostructure comprising two Bernal-stacked bilayer graphene (BLG) sheets separated by a 2.5 nm hexagonal boron nitride (hBN) spacer in the quantum Hall (QH) regime. Using top and bottom gate control, together with an interlayer bias, we independently tune the two BLG layers into either the lowest ($N = 0$) or second ($N = 1$) Landau level (LL) orbital and probe their interlayer QH states. When both layers occupy the $N = 0$ orbital, we observe both interlayer exciton condensates (ECs) at integer total filling and interlayer fractional QH states, echoing the results in double monolayer graphene. In contrast to previous studies, however, when both BLG layers occupy the $N = 1$ orbital, we also observe quantized drag signals, signifying an interlayer exciton condensate formed between the second LLs. By tuning the layer degree of freedom, we find that this $N = 1$ EC state arises only when the $N = 1$ wavefunction in each BLG is polarized toward the hBN interface to maximize the interlayer Coulomb interaction.

Electrons moving in two-dimensional (2D) space and under a strong magnetic field fall into discrete Landau levels (LLs), indexed by an orbital quantum number $N = 0, 1, 2, \dots$, with the corresponding spatial wavefunction becoming increasingly nodal as N increases. The ultraflat electronic dispersion creates an ideal environment for Coulomb interactions to dominate and induce various many-body ground states, such as the Wigner crystal [1], charge density wave [2], and most notably, the fractional quantum Hall (FQH) effect [3], where quasiparticles with fractional charge and statistics emerge. The orbital character is critical to interaction physics because the Haldane pseudopotential for LL wavefunctions varies with N [4]. In particular, even-denominator FQH states at half-filling have been predominantly observed in the $N = 1$ LL [5–10], and are believed to be described by a class of non-Abelian states including the Moore-Read Pfaffian state [11]. There is also numerical evidence showing that composite fermion pairing is favored here due to the softened Coulomb repulsion, unlike in $N = 0$ [12]. Experimentally, access to different LLs effectively serves as a powerful tuning knob for electron-electron interactions, fostering exotic many-body phases.

Quantum Hall (QH) physics can be further enriched by placing two electrically isolated, parallel layers of 2D electron systems close to each other so that electrons in one layer interact

* zeyuh@berkeley.edu

† philipkim@g.harvard.edu

solely through Coulomb interaction with those in the other. This double-layer structure enables more complex multi-component states by introducing a new pseudospin — the layer index, and provides unique experimental access to coherent QH states by allowing for probing the two spatially separated pseudospin components, something impossible for a spin or valley based multi-component state. In particular, the multi-component Halperin (111) state [13] composed of layer pseudospins maps to an interlayer exciton condensate (EC) formed from electrons and holes in the partially filled LLs in the opposite layers [14, 15]. Such interlayer ECs were first observed in GaAs double quantum wells [16, 17], and later realized in double layer structures of monolayer or Bernal-stacked bilayer graphene (BLG) [18–21]. The exceptional flexibility and tunability of these double-layer graphene structures further enabled observation of the BEC-BCS crossover [22], novel interlayer FQH states [20, 21] and exciton solids [23].

However, all of these interlayer states have only been observed when both layers are in the $N = 0$ LL; no such states have been detected between the $N = 1$ LLs in graphene double-layer structures. Since $N = 1$ can host a different hierarchy of single-layer FQH states, it could likewise support qualitatively new interlayer states in double-layer systems. Furthermore, once an EC between two $N = 1$ LLs is realized, the transition between this interlayer coherent EC and individual-layer even-denominator FQH states could be a highly nontrivial topological phase transition [24, 25]. Previously, there have been reports of gapped states in 2H-stacked bilayer WSe₂ [26] or twisted double bilayer graphene [27] that are consistent with interlayer ECs in higher LLs. However, while the absence of a spacer helps achieve strong interlayer coupling, it prevents probing each layer pseudospin separately, making it impossible to conclusively identify the interlayer coherence of EC states. In this Letter, we present the first observation of quantized Coulomb-drag signals between the $N = 1$ LLs in a double bilayer graphene device, providing key signatures of EC formation in higher LLs.

Fig. 1a shows the image of the device, and Fig. 1b illustrates its layer configuration. The device fabrication processes are similar to those in our previous studies [20, 21]. Briefly, two BLG layers are stacked on top of each other separated by a 2.5 nm thick hBN spacer. They are further encapsulated by layers of hBN and graphite from both top and bottom, with the graphite layers acting as local top and bottom gates. Separate gold contacts are made to the top and bottom BLGs where they do not overlap. To ensure good equilibrium between the

gold contacts and the channel region, we utilize the global silicon back gate and fabricate additional aluminum oxide dielectric layers with patterned gold contact gates on top of the heterostructure to heavily dope the top and bottom graphene leads.

The phase diagram of BLG at high magnetic fields is determined by the displacement field and carrier density. When higher-order energy anisotropies are ignored, the zero-energy LL of BLG consists of eight quasi-degenerate flavors: spin up and down, valley K and K' , and an orbital quantum number, $N = 0$ and 1 [28]. Fig. 1c illustrates the latter two flavors. The $N = 0$ orbital in BLG has a LL wavefunction similar to the lowest LL in a conventional quadratic-band system like GaAs. By contrast, the $N = 1$ orbital in BLG is an admixture of the conventional lowest and second LL wavefunctions [28]. Depending on the valley flavor, these wavefunctions are layer-polarized within BLG, as shown in Fig. 1c. Previous studies on QH states in BLG have shown that next-order energy anisotropies and Coulomb interaction induce an energy hierarchy among the eight flavors, leading to their sequential filling as carrier density increases [8, 9, 29]. A displacement field further modifies the hierarchy by shifting the relative potential of the two graphene layers within the BLG and alters the energetics of the eight flavors due to their varying degrees of layer polarization.

In our experiment, by applying DC voltages to the top and bottom graphite gates, V_{TG} and V_{BG} , as well as between the two BLG layers V_{int} (with the bottom BLG grounded), we can control the carrier density and displacement field in each BLG, and selectively tune them into different flavor polarization states. More specifically, the carrier densities are given by $n_{\text{top}} = \frac{1}{e}(C_{\text{t}}(V_{\text{TG}} - V_{\text{int}}) - C_{\text{int}}V_{\text{int}})$ and $n_{\text{bot}} = \frac{1}{e}(C_{\text{b}}V_{\text{BG}} + C_{\text{int}}V_{\text{int}})$, and the displacement fields $D_{\text{top}}/\epsilon_0 = \frac{1}{2}(C_{\text{t}}(V_{\text{TG}} - V_{\text{int}}) + C_{\text{int}}V_{\text{int}})$ and $D_{\text{bot}}/\epsilon_0 = \frac{1}{2}(-C_{\text{b}}V_{\text{BG}} + C_{\text{int}}V_{\text{int}})$. Here, e is the electron charge, ϵ_0 is the vacuum permittivity, and C_{t} , C_{int} and C_{b} are the geometric capacitances between the top graphite and top BLG, between the top and bottom BLG layers, and between the bottom BLG and bottom graphite, respectively (see Supplementary Information (SI) S1). Similar to our previous experiment [20], we measure the longitudinal/Hall resistance of both the drive/drag layers $R_{\text{drive/drag}}^{\text{xx/xy}}$. A nontrivial drag signal often provides an unambiguous indication of an interlayer state. Unless otherwise specified, most of the data presented in the main text were acquired with the bottom BLG as the drive layer and the top BLG as the drag layer at temperature $T = 250$ mK and magnetic field $B = 16$ T.

We first examine the QH phase diagram of the bottom BLG by fixing V_{TG} to zero and

sweeping only V_{int} and V_{BG} . In this configuration, we effectively use the top BLG as a top gate for the bottom BLG. Fig. 1d shows $R_{\text{xx}}^{\text{drive}}$ as a function of D_{bot} , and the LL filling factor, $\nu_{\text{bot}} = n_{\text{bot}}/n_0$, where $n_0 = eB/h$ is the LL degeneracy per unit area. The range of ν_{bot} spans from -2 to 4, covering a substantial portion of the zero-energy LL manifold. Generally, we observe vertical features that are consistent with previous studies. The large regions of zero $R_{\text{xx}}^{\text{drive}}$, shown in deep blue near integer ν_{bot} , correspond to the integer QH states. The resistive regions in between indicate partially filled LLs. The data show two distinct types of partially filled LLs: one characterized by sharp resistance minima, which are indicative of FQH states with a denominator of 3 and appear mainly between $0 < \nu_{\text{bot}} < 1$ and $2 < \nu_{\text{bot}} < 3$. This is characteristic of the $N = 0$ LL orbitals in BLG. The other type corresponds to the partially filled $N = 1$ LL, which lacks such fractional features with vanishing $R_{\text{xx}}^{\text{drive}}$, and predominantly appears in the range $1 < \nu_{\text{bot}} < 2$ and $3 < \nu_{\text{bot}} < 4$.

In addition to the QH states, we also observe several resistive horizontal lines indicative of phase transitions at constant D_{bot} . Prominent examples lie at $D_{\text{bot}}/\epsilon_0 \approx 0$ across the full ν_{bot} range and at $D_{\text{bot}}/\epsilon_0 \approx \pm 100$ mV/nm near $\nu_{\text{bot}} = 1$. There are subtler transition lines that become more visible in the numerical derivative of the data (see SI S3). These features originate from ground state rearrangement induced by changes in the QH state hierarchy. In Fig. 1e, we illustrate these features as dashed horizontal lines, together with solid lines that mark the FQH states and the boundaries of integer QH states. This phase diagram matches the previously studied BLG flavor transition maps obtained at comparable magnetic fields [8, 29]. Based on this comparison, we can precisely assign the flavor polarization to each LL segment in Fig. 1e, with the same color coding as Fig. 1c for different valley and orbital flavors. We also note that the phase boundaries between different LLs exhibit zigzag shapes. This irregularity occurs because as V_{int} changes, the top BLG intermittently enters its own gapped QH states and momentarily stops to act as a gate.

Setting $V_{\text{int}} = 0$, we now tune ν_{top} and ν_{bot} independently via V_{TG} and V_{BG} and study the collective phase diagram of the two BLG layers. Fig. 2a and 2b show $R_{\text{xx}}^{\text{drive}}$ and the corresponding R_{xx}^{drag} over $-4 \leq \nu_{\text{top}} \leq 4$ and $0 \leq \nu_{\text{bot}} \leq 4$. The vertical stripe features are primarily QH states of the drive layer — the bottom BLG. Based on the aforementioned denominator-3 FQH features, we can already infer that the bottom BLG occupies $N = 0$ LL for $0 \leq \nu_{\text{bot}} \leq 1$ and $2 \leq \nu_{\text{bot}} \leq 3$, and $N = 1$ LL for $1 \leq \nu_{\text{bot}} \leq 2$ and $3 \leq \nu_{\text{bot}} \leq 4$. This assignment is confirmed by computing the corresponding D_{bot} (see SI Fig. S5c) and

comparing with the single-layer BLG phase diagram. Similar analysis shows that the top BLG resides in $N = 0$ LL for ν_{bot} intervals $[-4, -3]$, $[-2, -1]$, $[0, 1]$, $[2, 3]$, and in $N = 1$ LL elsewhere. The zigzag shape of the vertical stripes again reflects the quantitative chemical potential change in the top BLG (see discussions in SI S3).

Beyond the intralayer QH features, we also observe interlayer features, highlighted by the eight dashed squares in Fig. 2a and 2b. These features arise only when both BLG layers occupy $N = 0$ LL, and they manifest as diamond-shaped features with a diagonal stripe running along lines of constant integer total filling $\nu_{\text{tot}} = \nu_{\text{top}} + \nu_{\text{bot}}$. Along each diagonal line, the number of quasi-holes in one layer equals to the number of quasi-electrons in the other. Furthermore, when $\nu_{\text{top}} > 0$ and $\nu_{\text{bot}} > 0$, the diagonal stripes appear as resistance minima approaching zero in both $R_{\text{xx}}^{\text{drag}}$ and $R_{\text{xx}}^{\text{drive}}$, while their $R_{\text{xy}}^{\text{drag}}$ and $R_{\text{xy}}^{\text{drive}}$ lock to the quantized value $\frac{1}{\nu_{\text{tot}}} \frac{h}{e^2}$. These signatures are consistent with the ECs in the previous Coulomb-drag studies of double monolayer graphene [20, 21] and double BLG [18, 19]. Fig. 2c and 2d zoom into the region around $(\nu_{\text{bot}}, \nu_{\text{top}}) = (0.5, 2.5)$ at $B = 16$ T and 25 T, respectively, and Fig. 2e around $(0.5, 0.5)$, all clearly revealing a wide region of zero $R_{\text{xx}}^{\text{drag}}$ along the diagonal. An off-diagonal line cut taken along $\nu_{\text{bot}} = \nu_{\text{top}} - 2$ (Fig. 2f) shows that exactly at $(\nu_{\text{bot}}, \nu_{\text{top}}) = (0.5, 2.5)$, where the EC occurs, $R_{\text{xx}}^{\text{drag}} = R_{\text{xx}}^{\text{drive}} = 0$ and $R_{\text{xy}}^{\text{drag}} = R_{\text{xy}}^{\text{drive}} = \frac{1}{3} \frac{h}{e^2}$.

What's also prominent in these diamond-shaped regions are the correlated fractional states of both intra- and interlayer nature. For example, the vertical streaks of $R_{\text{xx}}^{\text{drag}} = 0$ at $\nu_{\text{bot}} = \frac{2}{3}$ in Fig. 2c and 2e, as well as the horizontal streaks of $R_{\text{xx}}^{\text{drag}} = 0$ at $\nu_{\text{top}} = 2 + \frac{2}{3}$ in Fig. 2c and $\nu_{\text{top}} = \frac{2}{3}$ in Fig. 2e correspond to intra-layer FQH states that developed independently in each BLG. There are also $R_{\text{xx}}^{\text{drag}}$ peaks that follow fractional-slope lines corresponding to interlayer FQH states, including $\nu_{\text{bot}} + \frac{2(\nu_{\text{top}}-2)}{3} = 1$ and $\nu_{\text{bot}} + \frac{3(\nu_{\text{top}}-2)}{5} = 1$ in Fig. 2c, and $\nu_{\text{bot}} + \frac{2\nu_{\text{top}}}{3} = 1$, $\nu_{\text{bot}} + \frac{\nu_{\text{top}}}{3} = 1$ and $\frac{\nu_{\text{bot}}}{3} + \nu_{\text{top}} = 1$ in Fig. 2e (see details in SI Fig. S8-S10). At higher magnetic fields, additional intra- and interlayer FQH states emerge. For example, compared to 16 T (Fig. 2c), the data at 25 T (Fig. 2d) presents additional intralayer FQH states at $\nu_{\text{top}/\text{bot}} = \frac{1}{3}, \frac{3}{5}$, and interlayer FQH states along $\frac{3\nu_{\text{bot}}}{2} + (\nu_{\text{top}} - 2) = 1$ and $\nu_{\text{bot}} + \frac{3(\nu_{\text{top}}-2)}{2} = 1$. These interlayer FQH states with fractional slopes, termed semi-quantized states, have been previously seen in double monolayer graphene [20] and are attributed to electrons binding interlayer vortices via interlayer Coulomb interactions. The fact that these interlayer FQH states appear in $N = 0$ LL but not $N = 1$ in double BLG mirrors the behavior of double monolayer graphene [20, 21], suggesting that the interlayer

FQH state structure depends more on the LL wavefunction than on the host material itself.

Despite the rich structure at $V_{\text{int}} = 0$, no interlayer states involving $N = 1$ LLs are seen. This changes when we introduce a finite interlayer bias. Fig. 3a and 3b present $R_{\text{xx}}^{\text{drive}}$ and the corresponding $R_{\text{xx}}^{\text{drag}}$ at $V_{\text{int}} = 0.07$ V. Now the $N = 0$ diamond features, again marked by dashed squares, survive only near four locations: $(\nu_{\text{bot}}, \nu_{\text{top}}) = (0.5, -1.5 \pm 2)$ and $(2.5, -1.5 \pm 2)$, and disappear near $(0.5, 0.5 \pm 2)$ and $(2.5, 0.5 \pm 2)$. Strikingly, new interlayer states emerge when the bottom BLG lies in $1 < \nu_{\text{bot}} < 2$ or $3 < \nu_{\text{bot}} < 4$ and the top BLG in $-3 < \nu_{\text{top}} < -2$ or $-1 < \nu_{\text{top}} < 0$, marked by dashed circles. Each appears as a diagonal minimum in $R_{\text{xx}}^{\text{drive}}$ along an integer ν_{tot} , accompanied by a non-zero drag signal, confirming their interlayer nature. Based on the QH phase diagram of single BLG, we can identify their locations as both layers occupying $N = 1$ LL. The two zoomed-in views overlaying Fig. 3a highlight the visual distinction between the previous $N = 0$ and the new $N = 1$ interlayer states. The $N = 0$ state on the left has a characteristic wide diagonal zero $R_{\text{xx}}^{\text{drive}}$ feature that cuts into the resistive region from one side and is surrounded by other fractional states. By contrast, the $N = 1$ state on the right manifests itself as a narrow zero $R_{\text{xx}}^{\text{drive}}$ line that cuts through the resistive region from both sides, without other prominent features in its surroundings. Raising V_{int} to 0.1 V reveals still more $N = 1$ interlayer states (see SI Fig. S7).

Although visually distinct, the $N = 1$ interlayer states show transport hallmarks of ECs: $R_{\text{xx}}^{\text{drag/drive}} = 0$ and $R_{\text{xy}}^{\text{drag/drive}} = \frac{1}{\nu_{\text{tot}}} \frac{h}{e^2}$. Fig. 3c and 3e display $R_{\text{xx}}^{\text{drag}}$ and $R_{\text{xy}}^{\text{drag}}$ for the $N = 1$ interlayer state near $(\nu_{\text{bot}}, \nu_{\text{top}}) = (1.5, 0.5)$ at $V_{\text{int}} = 0.1$ V. This interlayer state exhibits as a thin line of $R_{\text{xx}}^{\text{drag}}$ dip within a narrow resistive strip that runs along the diagonal, and as a peak in $R_{\text{xy}}^{\text{drag}}$ along the same line. Examining the off-diagonal linecut along $\nu_{\text{bot}} = \nu_{\text{top}} - 1$, we observe that at $(\nu_{\text{bot}}, \nu_{\text{top}}) = (1.5, 0.5)$, $R_{\text{xy}}^{\text{drag}}$ and $R_{\text{xy}}^{\text{drive}}$ approach the quantization value $\frac{1}{2} \frac{h}{e^2}$ (Fig. 3d), while $R_{\text{xx}}^{\text{drag}}$ and $R_{\text{xx}}^{\text{drive}}$ drop to 0 (Fig. 3f), consistent with an interlayer EC. Note that this $N = 1$ interlayer state appears for $V_{\text{int}} = 0.1$ V, but is absent in $V_{\text{int}} = 0.07$ V (Fig. 3b).

An interesting question is how to understand the strong V_{int} dependence of the $N = 1$ interlayer EC. We note that the interlayer bias allows us to independently tune D_{top} and ν_{top} in the top BLG while keeping the bottom BLG ν_{bot} constant (see SI S6 for details). Fig. 4a and 4b present 2D maps of $R_{\text{xx}}^{\text{drive}}$ and $R_{\text{xx}}^{\text{drag}}$, respectively, for fixed $\nu_{\text{bot}} = 3.5$, while

Fig. 4c shows R_{xx}^{drive} for fixed $\nu_{\text{bot}} = 1.5$. At these two fillings and given our sweeping ranges, we are keeping the bottom BLG mostly in $N = 1$ LLs (see SI S6). Fig. 4a and 4c both exhibit resistive patterns that are generally periodic in ν_{top} , reflecting the QH states of the top BLG that manifest in the bottom BLG R_{xx}^{drive} due to screening effects. This is illustrated in Fig. 4d as the four colored stripes bounded by solid lines. More importantly, Fig. 4a and 4c both exhibit four curved boundaries (represented as dashed lines in Fig. 4d) that cut through the repeating LL features near integer ν_{top} . These curves are consistent with the hierarchy transitions in the top BLG, allowing us to assign each LL section with colors corresponding to its valley flavor and orbital number defined in Fig. 1c.

Among these features, the $N = 1$ EC states manifest as non-zero drag resistance peaks in the otherwise mostly zero R_{xx}^{drag} (Fig. 4b) that align with the resistance dips in R_{xx}^{drive} (Fig. 4a and 4c). Note that an EC should exhibit zero resistance in both R_{xx}^{drag} and R_{xx}^{drive} . However, an imperfect positioning of ν_{bot} can shift R_{xx}^{drag} away from the narrow resistance dip and produce the peaks in Fig. 4b. In Fig. 4d, we represent the experimentally observed $N = 1$ EC states as thick solid lines. As can be seen immediately, these interlayer EC states occur only when the upper BLG is in the $N = 1$ orbital and K' valley. We can also demonstrate that, over the same range of gate parameters, the lower BLG remains $N = 1$ orbital and K valley (see SI S6). Being an admixture of the conventional lowest and second LL wavefunctions, the $N = 1$ orbital with K' (K) valley in the upper (lower) BLG has its second LL wavefunction component (also has a higher wavefunction weight) polarized to the bottom (top) graphene layer within the BLG (see the upper inset illustration in Fig. 4d). Taken together, our observations suggest that the $N = 1$ EC states select a particular flavor polarization so that the higher LL wavefunctions in the two BLGs lie in immediate proximity to each other across the hBN spacer.

Formation of an interlayer EC relies on the interlayer Coulomb interaction and therefore in principle favors bringing the active orbitals as close as possible provided there is no significant interlayer tunneling. However, switching layer polarization of a BLG orbital moves the wavefunction by only 0.34 nm, insignificant compared to the 2.5 nm hBN spacer that sets the interlayer Coulomb interaction scale. Geometric proximity alone is therefore unlikely to explain why the $N = 1$ EC selects a specific valley (or layer) flavor combination. A plausible mechanism likely involves the interlayer Haldane pseudopotential, which sensitively depends on the detailed wavefunction distributions. It is possible that the $N = 1$ EC is stabilized

only in configurations where the second LL component of the $N = 1$ LL in one BLG can interact directly with that in the other, free from screening by the co-existing lowest LL component.

In conclusion, we have mapped out the interlayer QH phase diagram of double bilayer graphene via Coulomb-drag transport. We observe the formation of interlayer ECs at integer total filling and fractional interlayer QH states when both BLG occupy $N = 0$ LLs. Crucially, we report the first observation of interlayer ECs within the $N = 1$ LL manifold backed by quantized Coulomb-drag signals. We have also identified the specific flavor combination required for the $N=1$ EC, revealing the important role of the interlayer Coulomb interaction. Moving forward, reducing the hBN spacer further and pushing to higher magnetic fields may reveal additional interlayer correlated states in the $N = 1$ orbital. On the other hand, realizing $N = 1$ interlayer ECs opens a pathway to exploring their potential exotic phase transitions to the intrinsic intralayer even-denominator FQH states in each individual BLG.

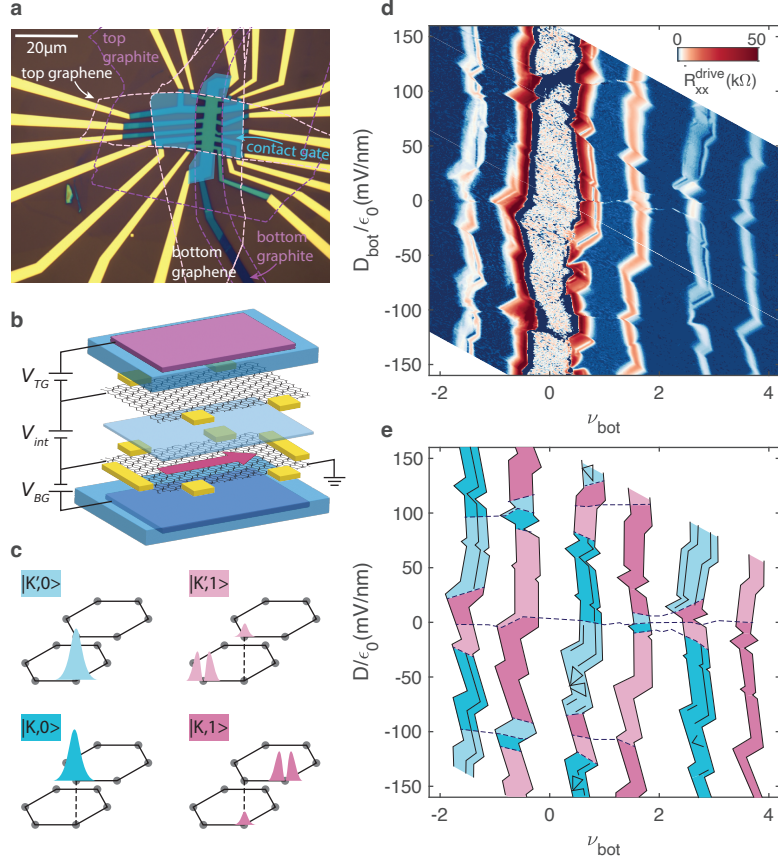


FIG. 1. **a**, Device picture with dashed lines denoting the original flake placement. The semi-transparent region is covered by contact gate. **b**, Schematic of the double layer structure and device configuration. **c**, Illustration of valley and orbital flavor of the zero-energy Landau levels in BLG. Spin flavor is not included. **d**, Drive resistance R_{xx}^{drive} (bottom layer) as a function of displacement field D_{bot} and filling factor ν_{bot} . **e**, Schematic of the main features in **d**.

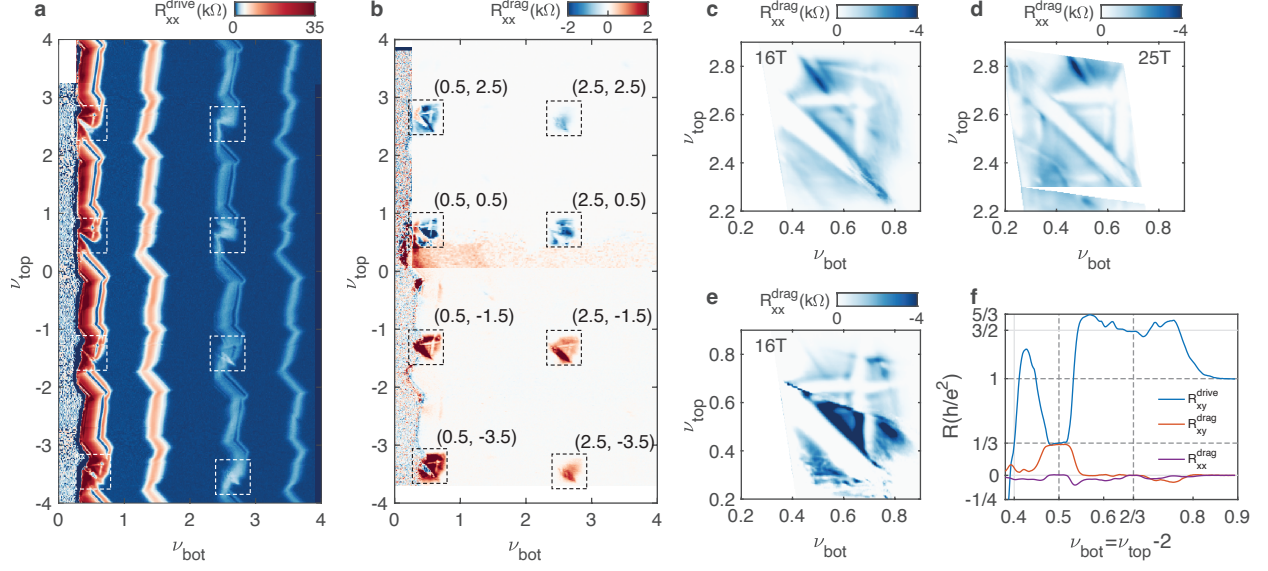


FIG. 2. **a**, R_{xx}^{drive} and **b**, R_{xx}^{drag} as a function of ν_{top} and ν_{bot} . **c**, R_{xx}^{drag} near $(\nu_{\text{top}}, \nu_{\text{bot}}) = (0.5, 2.5)$ at $B = 16$ T. **d**, same as **c** but with $B = 25$ T. **e**, R_{xx}^{drag} near $(\nu_{\text{top}}, \nu_{\text{bot}}) = (0.5, 0.5)$ at $B = 16$ T. **f**, Linecut across the EC state in **c** showing R_{xx}^{drag} as well R_{xy}^{drag} and R_{xy}^{drive} .

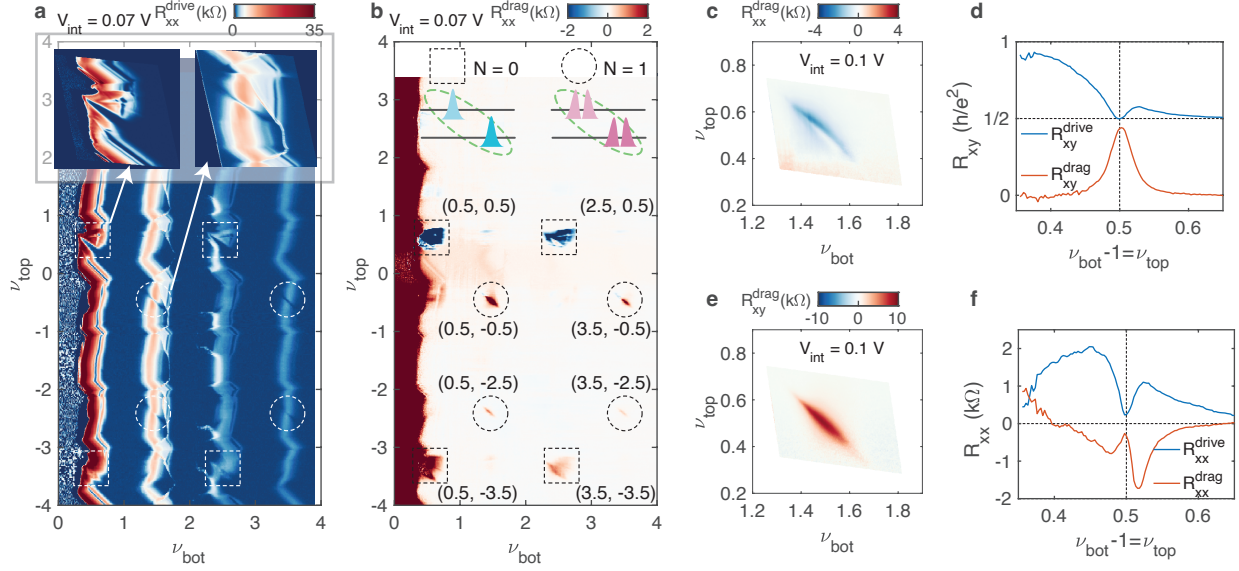


FIG. 3. **a**, R_{xx}^{drive} as a function of ν_{top} and ν_{bot} at $V_{\text{int}} = 0.07$ V. Dashed squares label interlayer states formed by $N = 0$ orbitals. Dashed circles marks the newly observe states formed by $N = 1$ orbitals. **b**, The corresponding drag signal R_{xx}^{drag} . The top insets show cartoons illustrating the two classes of interlayer states formed by coupling $N = 0$ and 1 LL orbitals. **c**, R_{xx}^{drag} and **e**, R_{xy}^{drag} near $(\nu_{\text{top}}, \nu_{\text{bot}}) = (1.5, 0.5)$ at $V_{\text{int}} = 0.1$ V. **d** and **f**, Linecuts across the state showing all other transport channels. Dashed lines denote the state location and quantization value.

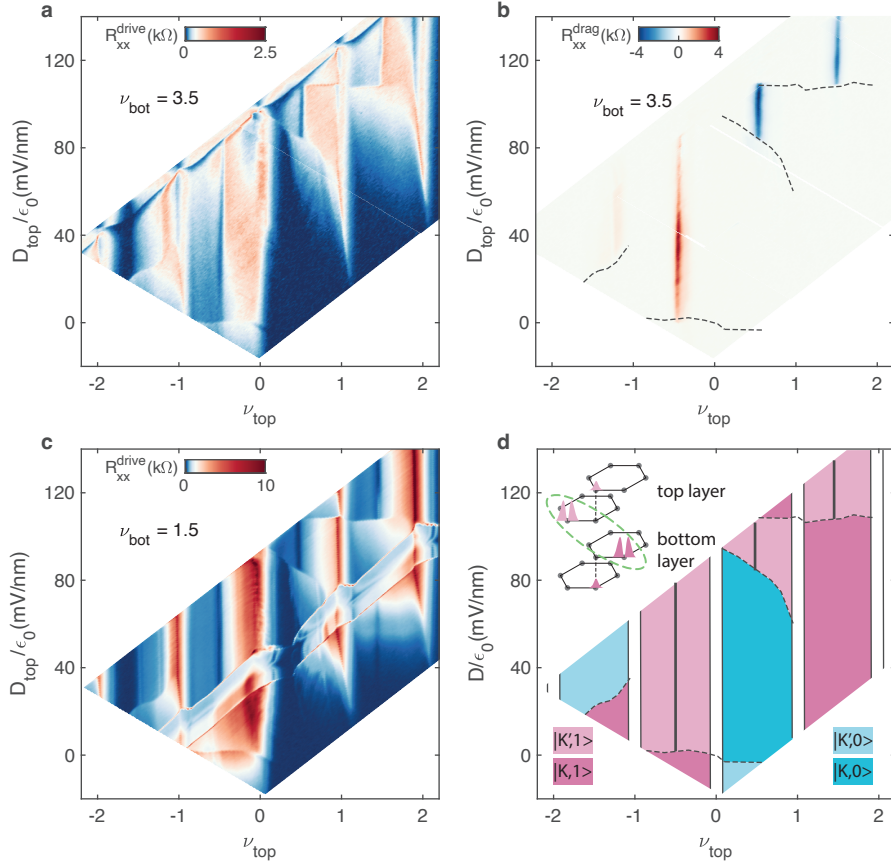


FIG. 4. **a**, $R_{\text{xx}}^{\text{drive}}$ at fixed $\nu_{\text{bot}} = 3.5$ as a function D_{top} and ν_{top} . **b**, $R_{\text{xx}}^{\text{drag}}$ in the same range. Showing clearly interlayer QH states. **c**, $R_{\text{xx}}^{\text{drive}}$ at fixed $\nu_{\text{bot}} = 1.5$. **d**, Schematic of the features in the resistance data. This shows the $N = 1$ interlayer QH states only forms when $N = 1$ orbitals are on the nearest layers.

Acknowledgment: The major part of the experiment was supported by the US Department of Energy (DOE) (DE-SC0012260). A portion of this work was performed at the National High Magnetic Field Laboratory, which is supported by National Science Foundation Cooperative Agreement No. DMR-2128556* and the State of Florida. K.W. and T.T. acknowledge support from the JSPS KAKENHI (grants 20H00354 and 23H02052) and World Premier International Research Center Initiative (WPI), MEXT, Japan.

-
- [1] H. A. Fertig, Properties of the Electron Solid, in *Perspectives in Quantum Hall Effects* (John Wiley & Sons, Ltd, 1996) pp. 71–108.
- [2] M. M. Fogler, Stripe and Bubble Phases in Quantum Hall Systems, in *High Magnetic Fields: Applications in Condensed Matter Physics and Spectroscopy* (Springer, Berlin, Heidelberg, 2001) pp. 98–138.
- [3] H. L. Stormer, The fractional quantum Hall effect, *Reviews of Modern Physics* **71**, S298 (1999).
- [4] F. D. M. Haldane, Fractional Quantization of the Hall Effect: A Hierarchy of Incompressible Quantum Fluid States, *Phys. Rev. Lett.* **51**, 605 (1983).
- [5] R. Willett, J. P. Eisenstein, H. L. Störmer, D. C. Tsui, A. C. Gossard, and J. H. English, Observation of an even-denominator quantum number in the fractional quantum hall effect, *Phys. Rev. Lett.* **59**, 1776 (1987).
- [6] W. Pan, J.-S. Xia, V. Shvarts, D. E. Adams, H. L. Stormer, D. C. Tsui, L. N. Pfeiffer, K. W. Baldwin, and K. W. West, Exact quantization of the even-denominator fractional quantum hall state at $\nu = 5/2$ Landau level filling factor, *Phys. Rev. Lett.* **83**, 3530 (1999).
- [7] J. Falson, D. Maryenko, B. Friess, D. Zhang, Y. Kozuka, A. Tsukazaki, J. H. Smet, and M. Kawasaki, Even-denominator fractional quantum Hall physics in ZnO, *Nature Phys* **11**, 347 (2015).
- [8] A. A. Zibrov, C. Kometter, H. Zhou, E. M. Spanton, T. Taniguchi, K. Watanabe, M. P. Zaletel, and A. F. Young, Tunable interacting composite fermion phases in a half-filled bilayer-graphene Landau level, *Nature* **549**, 360 (2017).
- [9] J. I. A. Li, C. Tan, S. Chen, Y. Zeng, T. Taniguchi, K. Watanabe, J. Hone, and C. R. Dean, Even-denominator fractional quantum Hall states in bilayer graphene, *Science* **358**, 648 (2017).
- [10] Q. Shi, E.-M. Shih, M. V. Gustafsson, D. A. Rhodes, B. Kim, K. Watanabe, T. Taniguchi, Z. Papić, J. Hone, and C. R. Dean, Odd- and even-denominator fractional quantum Hall states in monolayer WSe₂, *Nat. Nanotechnol.* **15**, 569 (2020).
- [11] G. Moore and N. Read, Nonabelions in the fractional quantum hall effect, *Nuclear Physics B* **360**, 362 (1991).
- [12] V. W. Scarola, K. Park, and J. K. Jain, Cooper instability of composite fermions, *Nature* **406**, 863 (2000).

- [13] B. I. Halperin, Theory of the quantized hall conductance, *Helvetica Physica Acta* **56**, 75 (1983).
- [14] G. S. Jeon and J. Ye, Trial wave function approach to bilayer quantum hall systems, *Phys. Rev. B* **71**, 035348 (2005).
- [15] H. A. Fertig, Energy spectrum of a layered system in a strong magnetic field, *Phys. Rev. B* **40**, 1087 (1989).
- [16] M. Kellogg, I. B. Spielman, J. P. Eisenstein, L. N. Pfeiffer, and K. W. West, Observation of quantized hall drag in a strongly correlated bilayer electron system, *Phys. Rev. Lett.* **88**, 126804 (2002).
- [17] D. Nandi, A. D. K. Finck, J. P. Eisenstein, L. N. Pfeiffer, and K. W. West, Exciton condensation and perfect Coulomb drag, *Nature* **488**, 481 (2012).
- [18] X. Liu, K. Watanabe, T. Taniguchi, B. I. Halperin, and P. Kim, Quantum Hall drag of exciton condensate in graphene, *Nature Physics* **13**, 746 (2017).
- [19] J. I. A. Li, T. Taniguchi, K. Watanabe, J. Hone, and C. R. Dean, Excitonic superfluid phase in double bilayer graphene, *Nature Phys* **13**, 751 (2017).
- [20] X. Liu, Z. Hao, K. Watanabe, T. Taniguchi, B. I. Halperin, and P. Kim, Interlayer fractional quantum Hall effect in a coupled graphene double layer, *Nat. Phys.* **15**, 893 (2019).
- [21] J. I. A. Li, Q. Shi, Y. Zeng, K. Watanabe, T. Taniguchi, J. Hone, and C. R. Dean, Pairing states of composite fermions in double-layer graphene, *Nat. Phys.* **15**, 898 (2019).
- [22] X. Liu, J. I. A. Li, K. Watanabe, T. Taniguchi, J. Hone, B. I. Halperin, P. Kim, and C. R. Dean, Crossover between strongly coupled and weakly coupled exciton superfluids, *Science* **375**, 205 (2022).
- [23] Y. Zeng, Q. Shi, A. Okounkova, D. Sun, K. Watanabe, T. Taniguchi, J. Hone, C. R. Dean, and J. I. A. Li, Evidence for a Superfluid-to-solid Transition of Bilayer Excitons (2023), arXiv:2306.16995 [cond-mat].
- [24] C. Shi, S. Jolad, N. Regnault, and J. K. Jain, Phase diagram for bilayer quantum hall effect at total filling $\nu_T = 5$, *Phys. Rev. B* **77**, 155127 (2008).
- [25] Z. Zhu, S.-K. Jian, and D. N. Sheng, Exciton condensation in quantum hall bilayers at total filling $\nu_T = 5$, *Phys. Rev. B* **99**, 201108 (2019).
- [26] Q. Shi, E.-M. Shih, D. Rhodes, B. Kim, K. Barmak, K. Watanabe, T. Taniguchi, Z. Papić, D. A. Abanin, J. Hone, and C. R. Dean, Bilayer WSe₂ as a natural platform for interlayer

- exciton condensates in the strong coupling limit, *Nat. Nanotechnol.* **17**, 577 (2022).
- [27] Q. Li, Y. Chen, L. Wei, H. Chen, Y. Huang, Y. Zhu, W. Zhu, D. An, J. Song, Q. Gan, Q. Zhang, K. Watanabe, T. Taniguchi, X. Shi, K. S. Novoselov, R. Wang, G. Yu, and L. Wang, Strongly coupled magneto-exciton condensates in large-angle twisted double bilayer graphene, *Nature Communications* **15**, 5065 (2024).
- [28] E. McCann and M. Koshino, The electronic properties of bilayer graphene, *Reports on Progress in Physics* **76**, 056503 (2013).
- [29] B. M. Hunt, J. I. A. Li, A. A. Zibrov, L. Wang, T. Taniguchi, K. Watanabe, J. Hone, C. R. Dean, M. Zaletel, R. C. Ashoori, and A. F. Young, Direct measurement of discrete valley and orbital quantum numbers in bilayer graphene, *Nature Communications* **8**, 948 (2017).

Supplementary Information

S1. CAPACITANCE MODEL

Fig. S1a shows the schematic diagram of the device again. $V_{\text{TG}}, V_{\text{BG}}, V_{\text{int}}$ are voltages applied to the top graphite gate, bottom graphite gate, and top bilayer graphene (BLG), respectively, with the bottom BLG grounded. Taking $V_{\text{est}}, V_{\text{esb}}$ and V_{esint} as electrostatic potential for the top, bottom, and interlayer capacitors, respectively, we have the following equilibrium equalities.

$$V_{\text{TG}} - V_{\text{int}} = V_{\text{est}} + \mu_t$$

$$V_{\text{BG}} = V_{\text{esb}} + \mu_b$$

$$V_{\text{int}} = V_{\text{esint}} + \mu_t - \mu_b$$

μ_t and μ_b are chemical potentials of the top and bottom BLG, respectively. The charge accumulation due to each electrostatic voltage term is $q_1 = C_t V_{\text{est}}, q_2 = C_b V_{\text{esb}}, q_3 = C_{\text{int}} V_{\text{esint}}$, and C_t, C_{int} and C_b are geometric capacitances between the top graphite and the top BLG, between the top and bottom BLG, and between the bottom BLG and bottom graphite, respectively. Then the general formulas relating the displacement field, carrier density, and chemical potential in each BLG with the gate voltages are as follows:

$$en_{\text{top}} = q_1 + q_3 = C_t(V_{\text{TG}} - V_{\text{int}} - \mu_t) + C_{\text{int}}(-V_{\text{int}} + \mu_b - \mu_t)$$

$$en_{\text{bot}} = q_2 - q_3 = C_b(V_{\text{BG}} - \mu_b) - C_{\text{int}}(-V_{\text{int}} + \mu_b - \mu_t)$$

$$D_{\text{top}} = \frac{-q_1 + q_3}{2} = \frac{1}{2}(-C_t(V_{\text{TG}} - V_{\text{int}} - \mu_t) + C_{\text{int}}(-V_{\text{int}} + \mu_b - \mu_t))$$

$$D_{\text{bot}} = \frac{q_2 + q_3}{2} = \frac{1}{2}(C_b(V_{\text{BG}} - \mu_b) + C_{\text{int}}(-V_{\text{int}} + \mu_b - \mu_t))$$

When determining the rough location in the displacement field-density map, we can often first ignore the chemical potential terms. Then the above formulas recover to the ones in the main text.

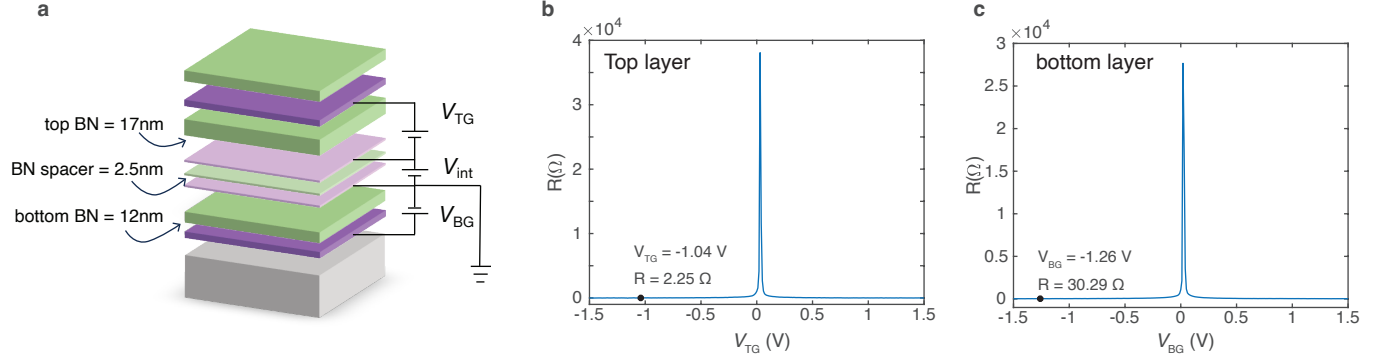


FIG. S1. **a**, device schematic showing thickness of the BN layers and gate configurations. **b** and **c**, resistance at zero magnetic field in the top and bottom layer respectively. The sharp charge neutrality peaks show the high quality of both of the two Bernal bilayer graphene layers.

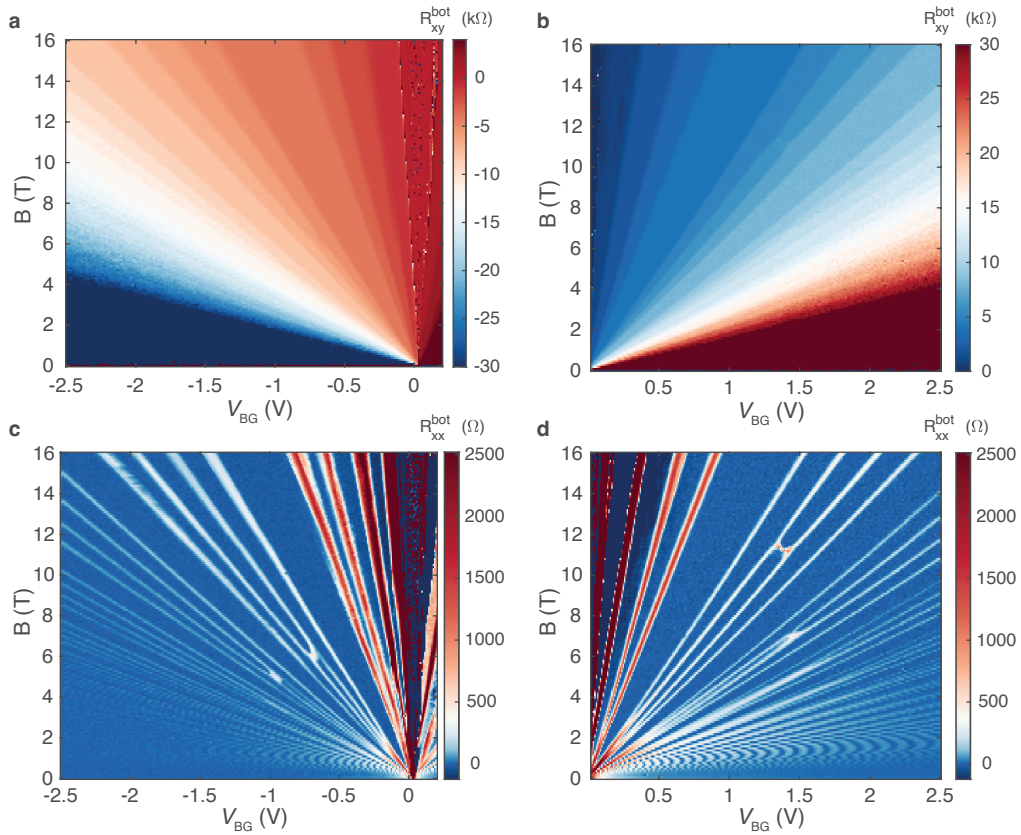


FIG. S2. Landau fan diagrams of the bottom layer as a function of V_{BG} . **a** and **b**, Hall resistance R_{xy} on the negative (hole-doped) and positive (electron-doped) V_{BG} side. **c** and **d**, longitudinal resistance R_{xx} .

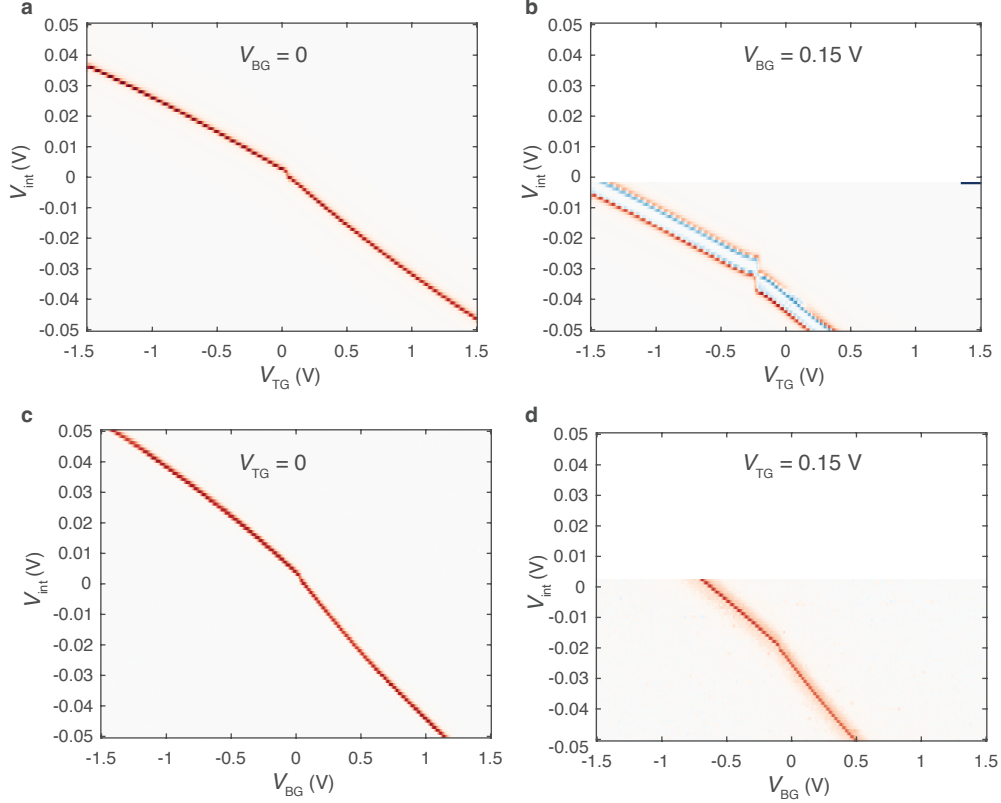


FIG. S3. BN spacer layer thickness extraction. **a** and **b**, R_{xx} in the top bilayer graphene as a function of V_{int} and V_{TG} , with V_{BG} fixed to 0 and 0.15 V, respectively. **c** and **d**, R_{xx} in the bottom bilayer graphene as a function of V_{int} and V_{BG} , with V_{TG} fixed to 0 and 0.15 V, respectively.

S2. ACCURATE EXTRACTION OF BN THICKNESS

Figs. S1b and c show the charge neutrality resistance peaks (CNPs) in the two BLG layers, respectively, where we measure their longitudinal resistance R_{xx} separately using only the top or bottom gate. The sharp peaks demonstrate the high quality of the individual BLG samples. Fig. S2 show transverse and longitudinal resistance R_{xy} and R_{xx} in the bottom layer. Clean data with good quantization in R_{xy} and the corresponding zero R_{xx} again demonstrate the high quality of the sample.

When converting the gate voltages to D or n associated with the BLG layers, it is important to know the thicknesses of the BN dielectric layers well. Although atomic force microscopy (AFM) can reliably measure relatively thick BN layers, giving the thickness of the top BN (between the top gate and top BLG) thickness ≈ 17 nm and bottom BN (between the bottom gate and bottom BLG) ≈ 12 nm, it can be difficult to accurately measure a thin

BN layer. In our experiment, we utilize the principle of measuring the chemical potential of one graphene layer using an adjacent graphene layer to extract the thickness of the BN spacer layer between layers.

Using the formulas we derived above and setting $n_{\text{bot}} = 0$ and $\mu_b = 0$, corresponding to staying at the charge neutrality of the bottom BLG, we obtain the following.

$$en_{\text{top}} = C_t V_{\text{TG}} + \frac{C_b(C_t + C_{\text{int}})}{C_{\text{int}}} V_{\text{BG}}$$

$$\mu_t = -V_{\text{int}} - \frac{C_b}{C_{\text{int}}} V_{\text{BG}}$$

These formulas mean that if we follow the CNP in the bottom BLG — for instance, the resistance peak in Fig. S3a and b — we can directly measure the n_{top} and μ_t at each point along the peak using the gate voltages at that point and geometric capacitance values. CNP peak in Fig. S3b is shifted to the lower left compared to Fig. S3a due to a finite V_{BG} . Using this shift, we can directly extract C_b/C_{int} using the formulas above and obtain an accurate value of the BN spacer layer thickness. Similarly, by tracking the CNP in the top layer, as shown in Fig. S3b and c, we can also extract C_t/C_{int} , allowing a consistent check of the relative thicknesses between the BN layers.

S3. ADDITIONAL DISCUSSION ON OUR MEASURED BLG QH PHASE DIAGRAM

In the main text, we discussed that the presence or absence of the the denominator-3 FQH state features provides a visual distinction can help us roughly identify the orbital number $N = 0$ or 1 for each region in the D versus ν phase diagram. However, more accurate identification of the orbital number relies on calculating D and ν , and using the QH phase diagram of single BLG as a reference, from which the flavors of both layers can be deduced.

Fig. S4 is presented from the same data as the Fig. 1d, but showing the numerical derivative $dR_{\text{xx}}^{\text{drive}}/d\nu_{\text{bot}}$ to make the features, especially the flavor transition features more prominent.

A key difference between our BLG phase diagram and previous studies is that we did not observe any even-denominator FQH states in $N = 1$ LLs. Given that the device is encapsulated by both top and bottom graphite gates and fabricated under the cleanest conditions possible, and considering that we observe interlayer FQH states as discussed

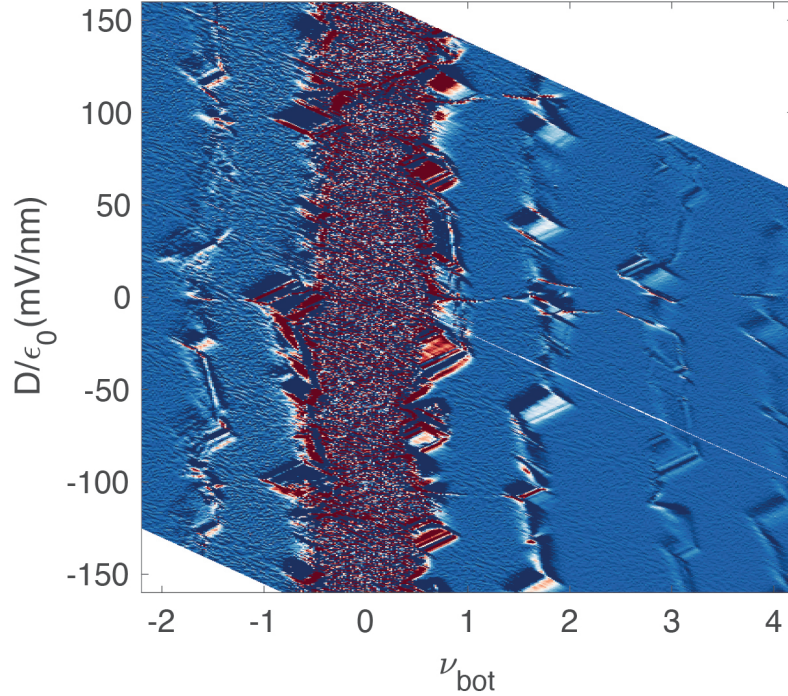


FIG. S4. Resistance derivative $dR_{xx}^{\text{drive}}/d\nu_{\text{bot}}$ corresponding to the data in Fig. 1d, more clearly showing quantum Hall state and hierarchy transition features.

later, the lack of even-denominator states is less likely due to sample quality but more likely due to the enhanced screening effects from the relatively thin hBN dielectric layers — top hBN is 12 nm ($12 \text{ nm}/l_B = 1.87$ at 16 T, $l_B = \sqrt{h/(2\pi eB)}$ is the magnetic length) and bottom hBN is 17 nm. Previous studies showing even-denominator FQH states generally used thicker (> 35 nm) hBN layers.

S4. ADDITIONAL DATA OF INTERLAYER QUANTUM HALL STATES

In the large 2D $\nu_{\text{bot}} - \nu_{\text{top}}$ maps, for instance, Fig 2a and 2b, although the two axes of this diagram, ν_{bot} and ν_{top} are nominally proportional to V_{BG} and V_{TG} when $V_{\text{int}} = 0$, the more accurate formula of $\nu_{\text{bot}} = n_{\text{bot}}/n_0$ includes chemical potentials: $n_{\text{bot}} = \frac{1}{e}(C_b V_{\text{BG}} - (C_b + C_{\text{int}})\mu_{\text{bot}} + C_{\text{int}}\mu_{\text{top}})$, where μ_{top} and μ_{bot} are the chemical potentials of top and bottom BLG layers, respectively. Therefore, if we follow a resistance feature of the bottom BLG that signals fixed n_{bot} and μ_{bot} , the V_{BG} value of that feature is directly proportional to μ_{top} . Indeed a negative slope in the $\nu_{\text{bot}} - \nu_{\text{top}}$ plane indicates a

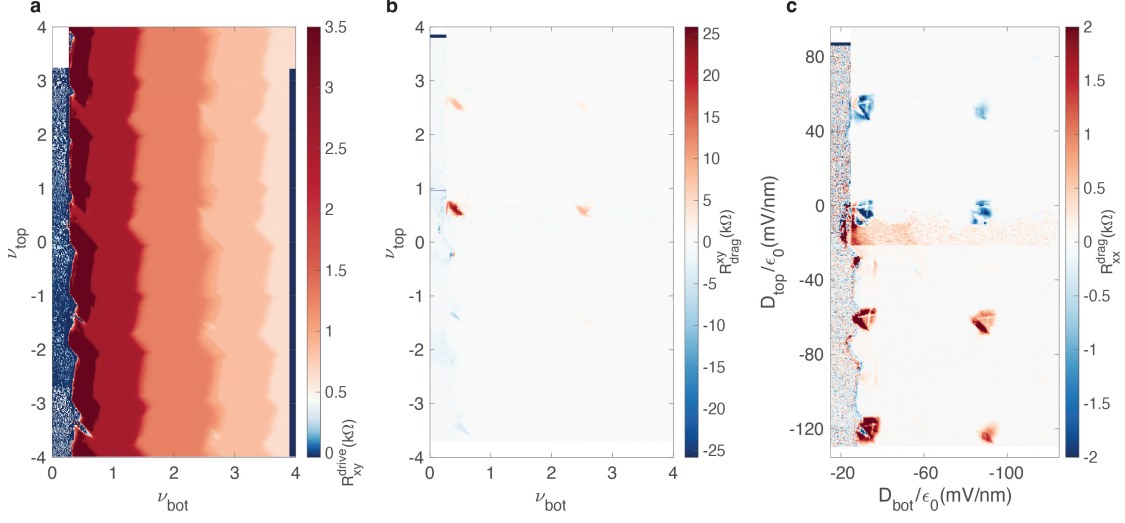


FIG. S5. Other resistance channels at $V_{\text{int}} = 0$. **a**, R_{xy}^{drive} . **b**, R_{xy}^{drag} . **c**, R_{xx}^{drag} plotted as a function of D_{top} and D_{bot} .

gapped state, where the chemical potential of top BLG suddenly shifts

Fig. S5 ($V_{\text{int}} = 0$) and S6 ($V_{\text{int}} = 0.07$ V) show complimentary resistance channels to those presented in Fig. 2 and Fig. 3 in the main text. Importantly, Fig. S5c and S6c plot the data as a function of the displacement fields of the top and bottom BLG. By reading off the corresponding $(D_{\text{bot}}, D_{\text{top}})$ and $(\nu_{\text{bot}}, \nu_{\text{top}})$ values for each interlayer state and consulting the single BLG phase diagram, we can unambiguously identify the flavor and orbital of each BLG underlying the interlayer state.

Fig. S7 shows all channels at $V_{\text{int}} = 0.1$ V, in which more $N = 1$ EC states emerge, marked by dashed circles.

S5. ADDITIONAL ZOOMED-IN VIEWS OF INTERLAYER STATES AND SEMI-QUANTIZED STATE ANALYSIS

Fig. S8-S12 are zoomed-in scans of various resistance channels for the $N = 0$ and $N = 1$ EC states, complementing the zoom-in scans shown in the main text Fig. 2 and 3. In particular, the dashed lines in all the e panels of Fig. S8-S10 illustrate the additional interlayer discussed in the main text. These lines well define linear relations with fractional slopes, corresponding to interlayer fractional states or the so-called semiquantized states.

We note that near $(\nu_{\text{bot}}, \nu_{\text{top}}) = (0.5, 0.5)$ at 16T (Fig. 2e in the main text and Fig. S10)

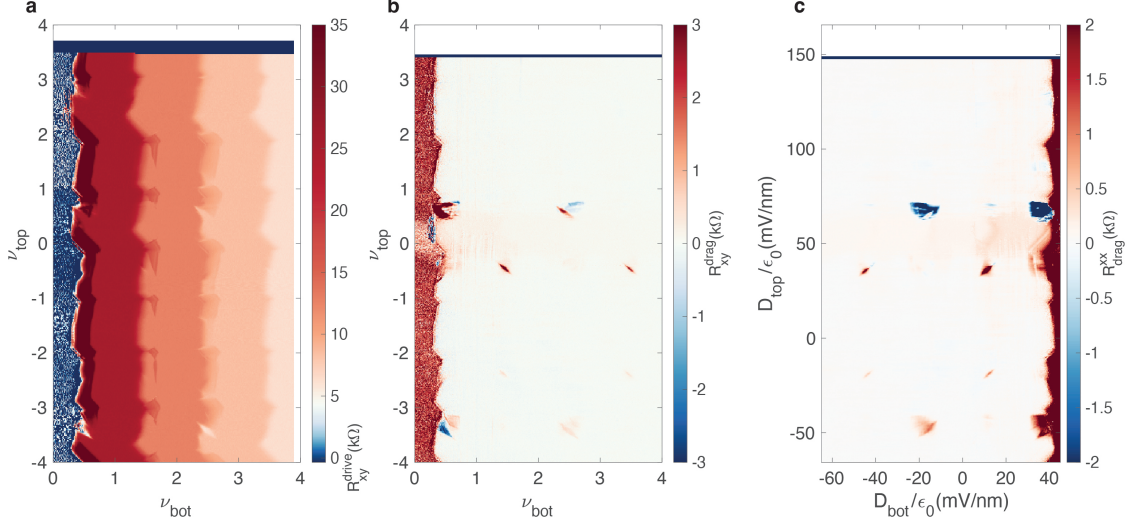


FIG. S6. Other resistance channels at $V_{\text{int}} = 0.07$ V. **a**, R_{xy}^{drive} . **b**, R_{xy}^{drag} . **c**, R_{xx}^{drag} plotted as a function of D_{top} and D_{bot} .

has an additional sharp transition in the middle of the structure. This occurs because the top BLG switches valley flavor here near zero D_{top} while remaining in the $N = 0$ orbital. Although there is an overall drop of R_{xx}^{drag} , the general state structure remains unchanged.

S6. ADDITIONAL DISCUSSION ON THE INTERLAYER BIAS DEPENDENCE

The idea behind using the V_{int} dependence to identify the existence conditions for the $N = 1$ interlayer EC states within the parameter space of $\nu_{\text{top/bot}}$ and $D_{\text{top/bot}}$ runs as follows. We first note that the $V_{\text{int}} = 0.07$ V data shown in Fig. 3a and 3b, as well as the $V_{\text{int}} = 0.1$ V data shown in Fig. S7, confirms that these $N = 1$ EC states can occur at $\nu_{\text{bot}} = 3.5$ or 1.5 . Then we simultaneously vary all three gates V_{TG} , V_{BG} and V_{int} while keeping the bottom filling fixed to $\nu_{\text{bot}} = 3.5$ or 1.5 . More precisely, we keep $V_{\text{BG}} + \frac{C_{\text{int}}}{C_{\text{b}}} V_{\text{int}}$ constant. The resulting 2D $V_{\text{TG}} - V_{\text{int}}$ (or equivalently $V_{\text{TG}} - V_{\text{BG}}$) map varies ν_{top} , D_{top} and D_{bot} , providing a direct visualization of how the $N = 1$ EC states form and evolve. It is more intuitive to convert the $V_{\text{TG}} - V_{\text{int}}$ map into an $n_{\text{top}} - D_{\text{top}}$ map, effectively generating a phase diagram of top layer bilayer graphene, as shown in main text Fig. 4.

Here in Figs. S13a and c, we plot the same R_{xx}^{drive} data as Fig. 4a and c in the main text, but as a function of V_{TG} and D_{bot} , so we can better identify the flavors transition features in the lower BLG. They can be easily identified as the features that are generally

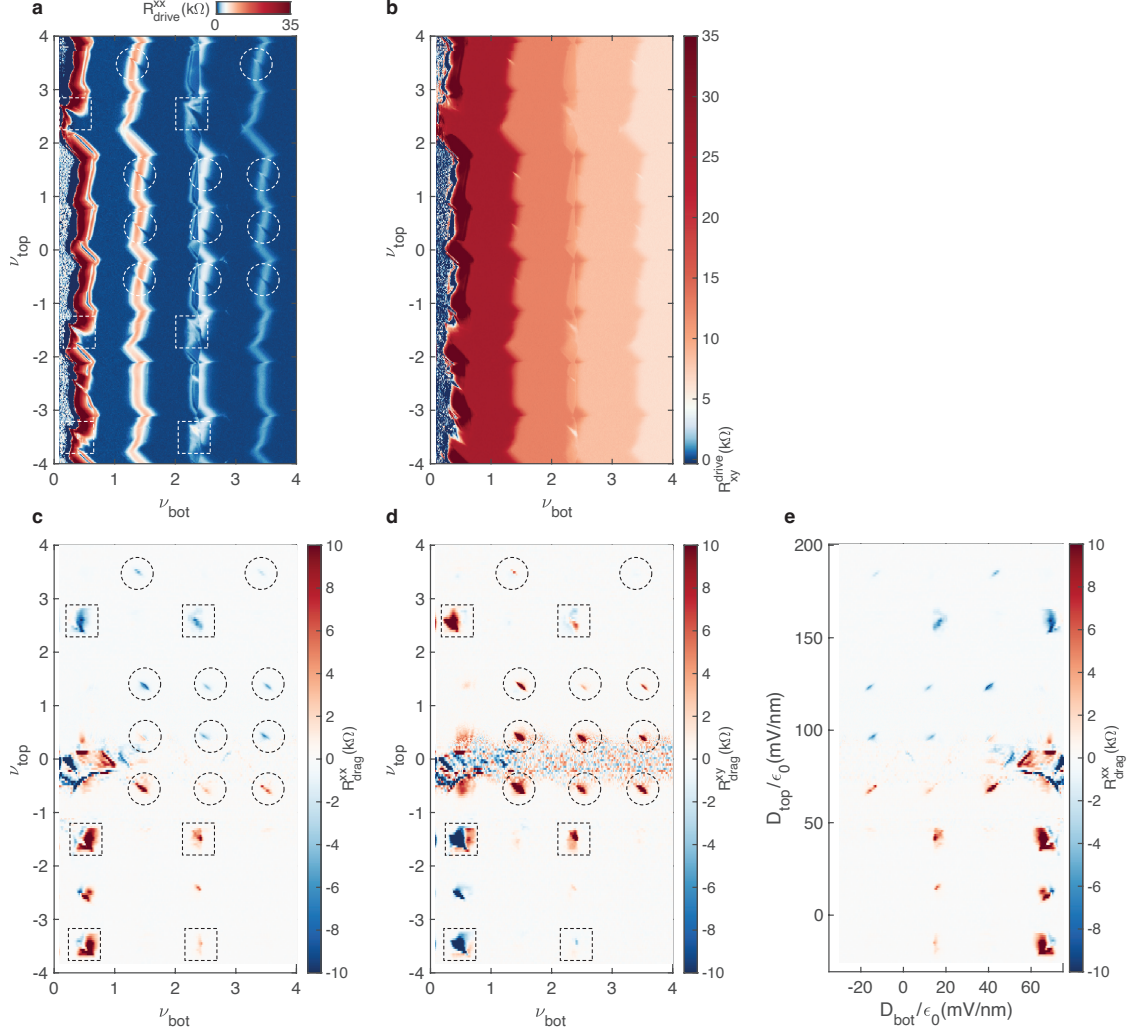


FIG. S7. All resistance channels at $V_{\text{int}} = 0.1$ V. **a**, $R_{\text{xx}}^{\text{drive}}$. **b**, $R_{\text{xy}}^{\text{drive}}$. **c**, $R_{\text{xx}}^{\text{drag}}$. **d**, $R_{\text{xy}}^{\text{drag}}$. **e**, $R_{\text{xx}}^{\text{drag}}$ plotted as a function of D_{top} and D_{bot} .

perpendicular to D_{bot} axis. Again, based on the phase diagram we obtained in Fig. 1e, here we similarly illustrate the bottom BLG LL in Figs. S13b and d, with each flavor colored following the same color scheme as in the main text, and dashed lines tracking the flavor transitions. Knowledge of the flavor distribution of the BLG confirms that the $N = 1$ EC states only appear when the $N = 1$ wavefunction is mostly populated in the top layer of the lower BLG.

Fig. S14 shows similar scans with the bottom bilayer graphene fixed to $\nu_{\text{bot}} = 2.5$, again consistent with our observation of the flavor combination required for $N = 1$ EC.

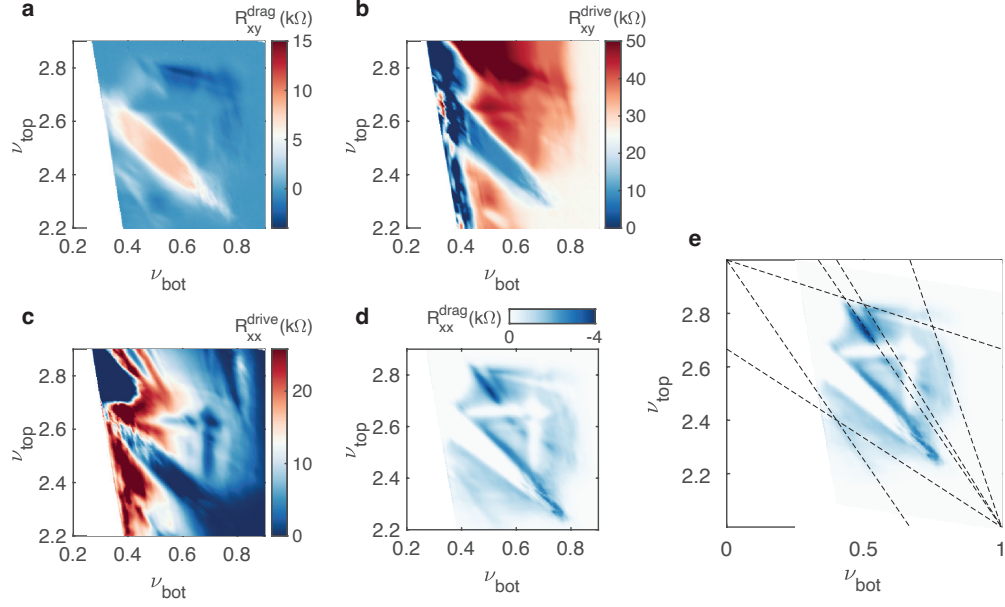


FIG. S8. Zoomed-in scans on the $N = 0$ interlayer states near $(\nu_{\text{bot}}, \nu_{\text{top}}) = (0.5, 2.5)$ at $V_{\text{int}} = 0$ and at 16 T. **a**, R_{xy}^{drag} . **b**, R_{xy}^{drive} . **c**, R_{xx}^{drive} . **d**, R_{xx}^{drag} , the same data as Fig. 2c in the main text. **e**, Dashed lines overlaid on top of the R_{xx}^{drag} data, marking interlayer fractional states, including $\nu_{\text{bot}} + \frac{2(\nu_{\text{top}}-2)}{3} = 1$, $\nu_{\text{bot}} + \frac{3(\nu_{\text{top}}-2)}{5} = 1$ and $\frac{\nu_{\text{bot}}}{3} + (\nu_{\text{top}} - 2) = 1$. There are subtle but less conclusive signals along $\nu_{\text{bot}} + \frac{(\nu_{\text{top}}-2)}{3} = 1$, $\nu_{\text{bot}} + \frac{3(\nu_{\text{top}}-2)}{2} = 1$ and $\frac{3\nu_{\text{bot}}}{2} + (\nu_{\text{top}} - 2) = 1$.

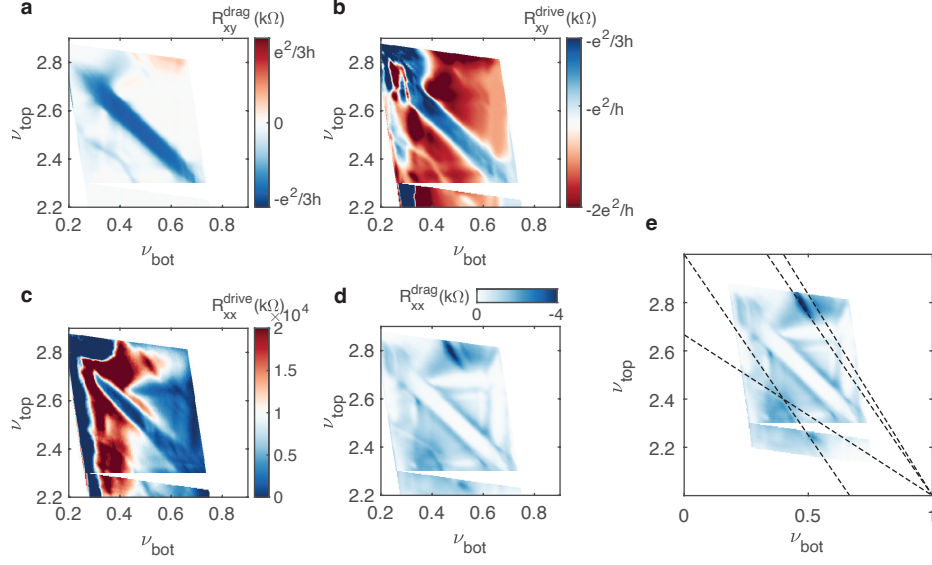


FIG. S9. Zoomed-in scans on the $N = 0$ interlayer states near $(\nu_{\text{bot}}, \nu_{\text{top}}) = (0.5, 2.5)$ at $V_{\text{int}} = 0$ and at 25 T. **a**, R_{xy}^{drag} . **b**, R_{xy}^{drive} . **c**, R_{xx}^{drive} . **d**, R_{xx}^{drag} , the same data as Fig. 2d in the main text. **e**, dashed lines overlaid on top of the R_{xx}^{drag} data, marking interlayer fractional states, including $\nu_{\text{bot}} + \frac{2(\nu_{\text{top}}-2)}{3} = 1$, $\nu_{\text{bot}} + \frac{3(\nu_{\text{top}}-2)}{5} = 1$, $\nu_{\text{bot}} + \frac{3(\nu_{\text{top}}-2)}{2} = 1$, $\frac{3\nu_{\text{bot}}}{2} + (\nu_{\text{top}} - 2) = 1$.

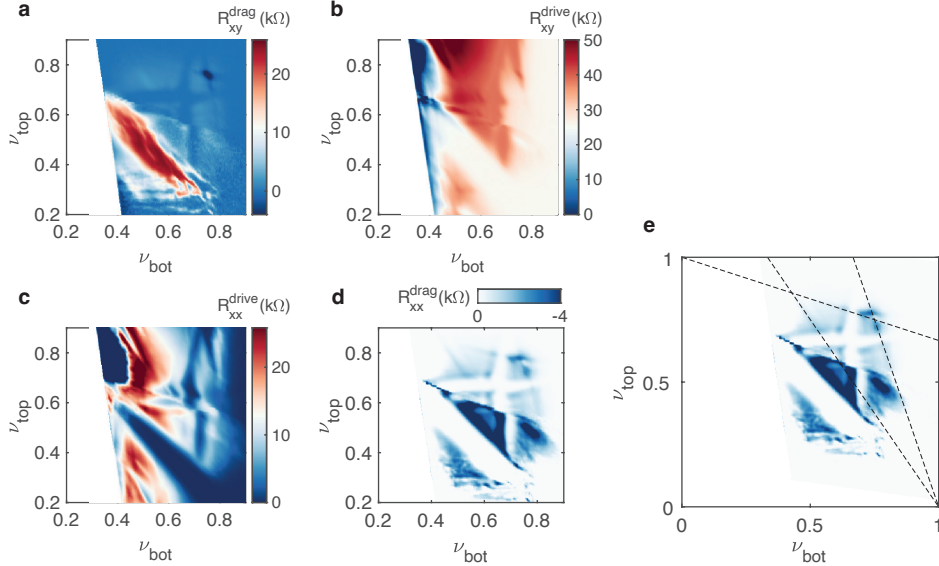


FIG. S10. Zoomed-in scans on the $N = 0$ interlayer states near $(\nu_{\text{bot}}, \nu_{\text{top}}) = (0.5, 0.5)$ at $V_{\text{int}} = 0$ and at 16 T. **a**, R_{xy}^{drag} . **b**, R_{xy}^{drive} . **c**, R_{xx}^{drive} . **d**, R_{xx}^{drag} , the same data as Fig. 2e in the main text. **e**, Dashed lines overlaid on top of the R_{xx}^{drag} data, marking interlayer fractional states, including $\nu_{\text{bot}} + \frac{2\nu_{\text{top}}}{3} = 1$, $\nu_{\text{bot}} + \frac{\nu_{\text{top}}}{3} = 1$ and $\frac{\nu_{\text{bot}}}{3} + \nu_{\text{top}} = 1$.

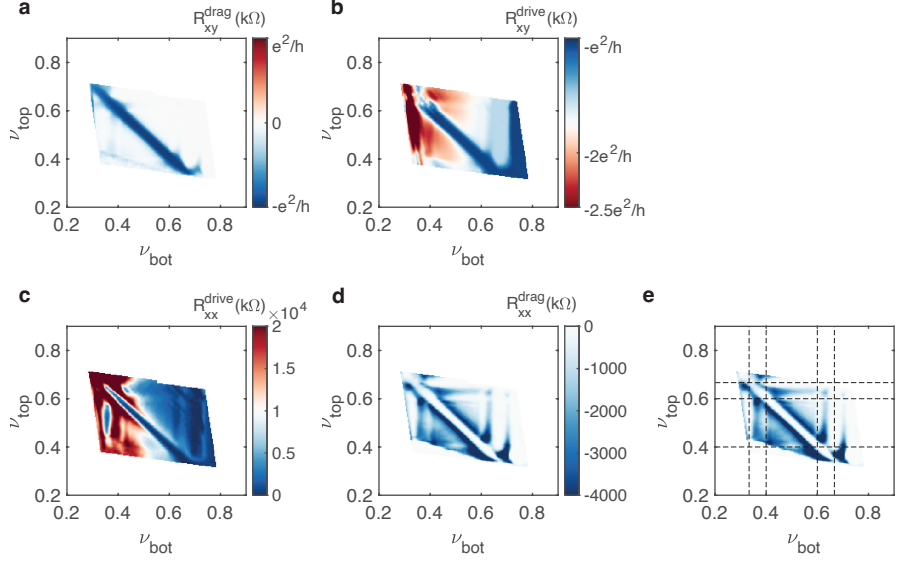


FIG. S11. Zoomed-in scans on the $N = 0$ interlayer states near $(\nu_{\text{bot}}, \nu_{\text{top}}) = (0.5, 0.5)$ at $V_{\text{int}} = 0$ and at 25 T. **a**, R_{xy}^{drag} . **b**, R_{xy}^{drive} . **c**, R_{xx}^{drive} . **d**, R_{xx}^{drag} . **e**, Dashed lines overlaid on top of the R_{xx}^{drag} data, marking the strong intralayer $1/3$, $2/3$, $2/5$, $3/5$ fraction quantum Hall states in both top and bottom BLG.

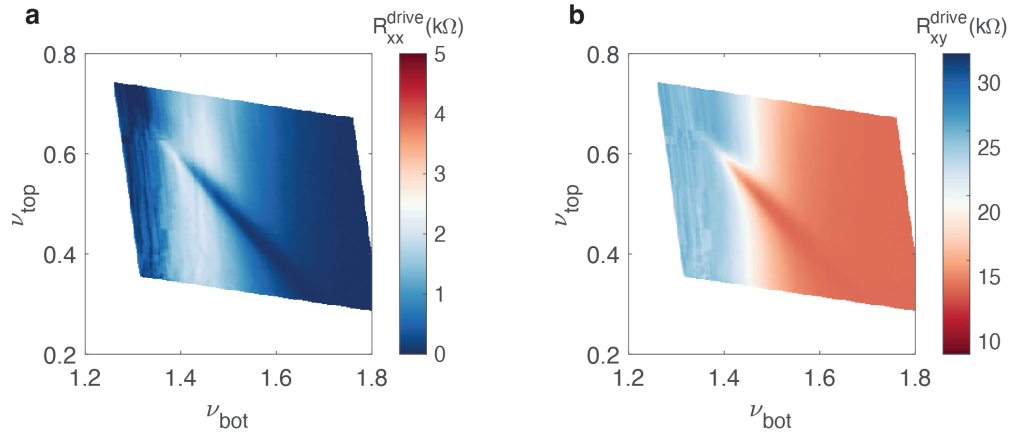


FIG. S12. Zoomed-in scans on the $N = 1$ interlayer states near $(\nu_{\text{bot}}, \nu_{\text{top}}) = (1.5, 0.5)$ at $V_{\text{int}} = 0.1$ V and at 16 T. **a**, R_{xx}^{drive} , **b**, R_{xy}^{drive} .

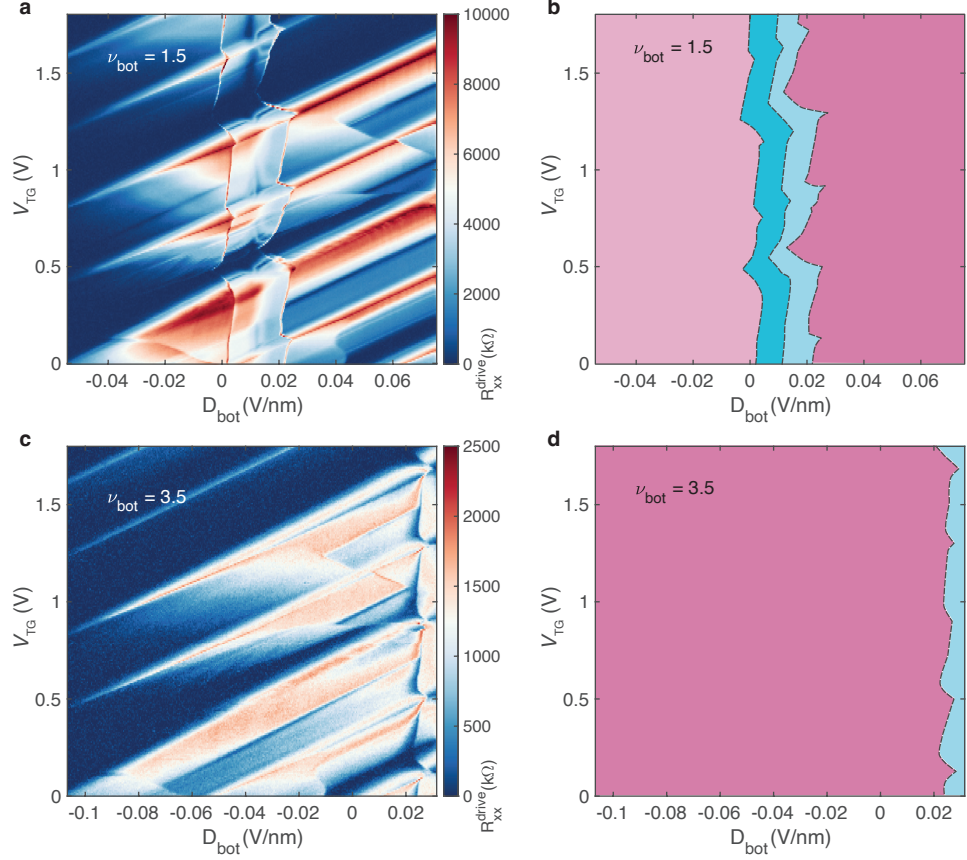


FIG. S13. **a** and **c**, R_{xx}^{drive} at fixed $\nu_{\text{bot}} = 1.5$ and 3.5 , respectively, as a function D_{bot} and V_{TG} . These are the same data as Fig. 4c and 4a in the main text but plotted against different axes. **b** and **d**, Schematics of the flavor transition features in the bottom BLG. Color shows different orbital and valley flavors, with the same color coding scheme as Fig.4 in main text.

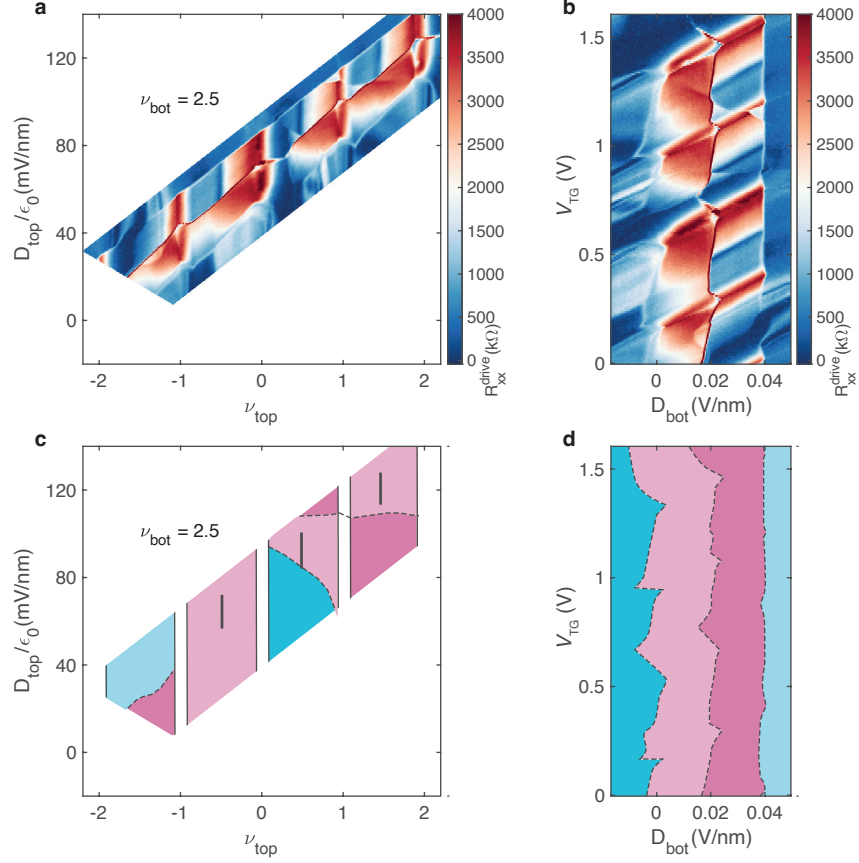


FIG. S14. R_{xx}^{drive} at fixed $\nu_{\text{bot}} = 2.5$, **a**, as a function D_{top} and ν_{top} , and **b**, D_{bot} and V_{TG} , respectively. **c**, Schematics of the features and flavors in the top BLG. **d**, Schematics of the features and flavors in the bottom BLG.